Particles-on-Demand for Kinetic Theory
Supplemental Material

B. Dorschner,* F. Bösch, and I. V. Karlin†
Department of Mechanical and Process Engineering, ETH Zurich, 8092 Zurich, Switzerland
(Dated: September 4, 2018)

EQUILIBRIUM

We consider the standard nine-velocity model, the $D2Q9$ lattice. The discrete speeds are constructed as a tensor product of two one-dimensional peculiar speeds, $c_i = i$, where $i = 0, \pm 1$. Discrete speeds in two-dimensions are

$$\boldsymbol{c}_{(i,j)} = (c_i, c_j)^\dagger, \tag{1}$$

where we have introduced two-dimensional indices in order to reflect the Cartesian frame instead of a more common single subscript. Thus, the discrete velocities are defined as

$$\boldsymbol{v}_{(i,j)} = \sqrt{\theta} \begin{pmatrix} c_i \\ c_j \end{pmatrix} + \begin{pmatrix} u_x \\ u_y \end{pmatrix}, \tag{2}$$

with reduced temperature $\theta = T/T_L$ and lattice temperature $T_L = 1/3$. Populations are labeled as well with two indices, $f_{(i,j)}$, corresponding to their respective velocities (2). The local equilibrium populations are now conveniently expressed as the product of one-dimensional weights

$$f^{\mathrm{eq}}_{(i,j)} = \rho W_{(i,j)} = \rho W_i W_j, \tag{3}$$

where

$$W_i = \begin{cases} 2/3, & \text{for } i = 0, \\ 1/6, & \text{otherwise.} \end{cases} \tag{4}$$

While the equilibrium populations are constant up to the proportionality to density, their moments

$$M^{\mathrm{eq}}_{mn} = \rho \sum_{(i,j)} W_i W_j (\sqrt{\theta} c_i + u_x)^m (\sqrt{\theta} c_j + u_y)^n, \tag{5}$$

recover the pertinent nine Maxwell-Boltzmann moments up to the fourth order, $0 \le m \le 2$, $0 \le n \le 2$, $m+n \le 4$, without error for any temperature and velocity.

TRANSFER MATRIX

Populations $f^\lambda_{(i,j)}$ measured in the gauge λ, can be represented as linear combinations of nine linearly independent moments,

$$M^\lambda = (M^\lambda_{00}, M^\lambda_{10}, M^\lambda_{01}, M^\lambda_{11}, M^\lambda_{20}, M^\lambda_{02}, M^\lambda_{21}, M^\lambda_{12}, M^\lambda_{22})^\dagger, \tag{6}$$

see also Eq. (2) in the main text, and $\mathcal{M}_\lambda$ is the $Q \times Q$ matrix of the linear map between populations and moments,

$$\mathcal{M}_\lambda f^\lambda = M^\lambda. \tag{7}$$

Moments are invariant with respect to the gauge,

$$\mathcal{M}_{\lambda'} f^{\lambda'} = \mathcal{M}_\lambda f^\lambda, \tag{8}$$

and the transfer from gauge λ to λ' can be written in the following explicit form,

$$f^{\lambda'}_{(k,l)} = \omega(k)\omega(l) \sum_{i,j} g_x(i,k) g_y(j,l) f^\lambda_{(i,j)}, \tag{9}$$

where

$$g_\xi(i,j) = A^2_\xi(i) - B_\xi(i,j), \tag{10}$$

$$A_\xi(i) = \left(u'_\xi - u_\xi\right)/\sqrt{3} - i\sqrt{T}, \tag{11}$$

$$B_\xi(i,j) = \begin{cases} T', & \text{for } j = 0, \\ j\sqrt{T'} A_\xi(i), & \text{otherwise,} \end{cases} \tag{12}$$

$$\omega(i) = \begin{cases} 1/T', & \text{for } i = 0, \\ -1/2T', & \text{otherwise.} \end{cases} \tag{13}$$

Formula (9) only involves evaluation of a dot-product as opposed to numerically solving the linear system (8).

RECONSTRUCTION

An equidistant rectilinear mesh with $\Delta x = 1$ is used for all simulations. Populations at off-grid locations are reconstructed using 3^{rd}-order polynomial interpolation,

$$\tilde{f}^\lambda_{(i,j)}(\boldsymbol{x}, t) = \sum_{\substack{0 \le m \le 3 \\ 0 \le n \le 3}} a_{mn}(\boldsymbol{x}) f^\lambda_{(i,j)}\left((x_0 + n, y_0 + m), t\right), \tag{14}$$

where the populations at integer collocation points $(x_0 + n, y_0 + m)$ are transformed to gauge λ using Eq. (9) and a_{mn} are standard Lagrange polynomials,

$$a_{mn}(\boldsymbol{x}) = \prod_{\substack{0 \le k \le 3 \\ k \ne n}} \frac{(x - x_0) - k}{n - k} \prod_{\substack{0 \le l \le 3 \\ l \ne m}} \frac{(y - y_0) - l}{m - l}, \tag{15}$$

with respect to reference coordinate,

$$\boldsymbol{x}_0 = (\lfloor x \rfloor - 1, \lfloor y \rfloor - 1), \tag{16}$$

where the operation $\lfloor \varphi \rfloor$ rounds down to the largest integer value not greater than φ.

HYDRODYNAMIC LIMIT

The single relaxation time D2Q9 BGK model recovers the Navier–Stokes–Fourier equations of the two-dimensional ideal gas:

$$\partial_t \rho + \nabla \cdot (\rho \boldsymbol{u}) = 0, \tag{17}$$

$$\partial_t \boldsymbol{u} + \boldsymbol{u} \cdot \nabla \boldsymbol{u} + \frac{1}{\rho}\nabla(\rho T) + \frac{1}{\rho}\nabla \cdot \boldsymbol{P}^{\rm neq} = 0, \tag{18}$$

$$\partial_t T + \boldsymbol{u} \cdot \nabla T + \frac{T}{C_v}\nabla \cdot \boldsymbol{u} + \frac{1}{\rho C_v}\nabla \boldsymbol{u} : \boldsymbol{P}^{\rm neq} + \frac{1}{\rho C_v}\nabla \cdot \boldsymbol{q}^{\rm neq} = 0, \tag{19}$$

where $C_v = D/2 = 1$ is the specific heat at constant volume, and the non-equilibrium pressure tensor and heat flux are, respectively

$$\boldsymbol{P}^{\rm neq} = -\mu\left(\nabla \boldsymbol{u} + \nabla \boldsymbol{u}^\dagger - \mathbf{1}\nabla \cdot \boldsymbol{u}\right), \tag{20}$$

$$\boldsymbol{q}^{\rm neq} = -\kappa \nabla T, \tag{21}$$

with the viscosity and thermal conductivity as

$$\mu = \rho T \delta t \left(\frac{1}{2\beta} - \frac{1}{2}\right), \tag{22}$$

$$\kappa = \frac{1}{2}\rho T \delta t \left(\frac{1}{2\beta} - \frac{1}{2}\right), \tag{23}$$

The BGK D2Q9 model presented in the paper thus recovers the correct temperature equation (19) for the two-dimensional ideal gas. One peculiarity of the thermal model on the D2Q9 lattice is the factor $1/2$ instead of 1 in the Fourier law of thermal flux (23), as first reported in the context of thermal LBGK [1]. Consequently, the Prandtl number for this model is fixed at

$$\Pr = \frac{C_p \mu}{\kappa} = \frac{(D+2)/2}{1/2} = 4, \tag{24}$$

and not at $\Pr = 1$, as in the conventional BGK.

In addition to validating the speed of sound ($c_{\rm s} = \sqrt{\gamma T}$, $\gamma = (D+2)/D = 2$, Figure 2 in the main text), the conduction of heat was probed by measuring thermal diffusivity from the decay of a sinusoidal temperature profile [2]. Theoretical prediction of thermal diffusivity for the present D2Q9 BGK model is (see (23), $C_p = (D+2)/2$, $D = 2$, $\delta t = 1$),

$$\alpha = \frac{\kappa}{\rho C_p} = \frac{T}{4}\left(\frac{1}{2\beta} - \frac{1}{2}\right). \tag{25}$$

Periodic set-up was chosen with an initial density $\rho = A\sin(2\pi x/L) + \rho_0$ at constant pressure $p = \rho_0 T_L$, with amplitude $A = 0.001$, $\rho_0 = 1$ and longitudinal resolution $L = 300$. Fig. 1 demonstrates excellent agreement between theory and numerical results, for a range of advection speed up to $\mathrm{Ma_a} = 100$, whereas thermal LBGK [1] shows severe deviations.

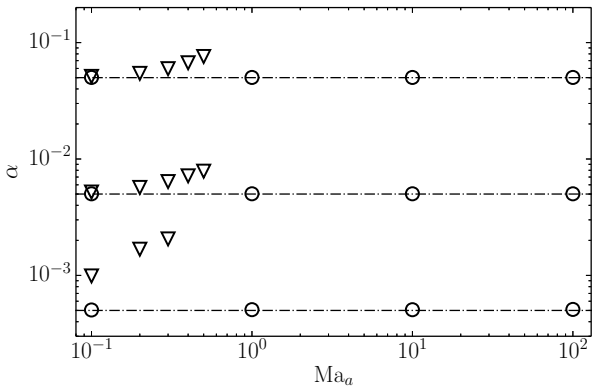

FIG. 1. Thermal diffusivity with the present $D2Q9$ BGK model at various advection Mach numbers $\mathrm{Ma}_a = u/\sqrt{2T}$. Line: theory (25); Circle: present method; Triangle: thermal LBGK [1].

EXPLANATION OF THE MOMENTS MATCHING CONDITION (3)

As in any gauge theory, the gauge-invariant property of the model is the cornerstone of the construction. Eq. (3) in the main text postulates gauge-invariance of all available moments, which is the same statement as in the continuous-velocity Boltzmann kinetic theory.

Let us use the notation, $\boldsymbol{v}^{\boldsymbol{n}} = \prod_{\alpha=1}^{D} v_\alpha^{n_\alpha}$, for any integer-valued vector $\boldsymbol{n}$, where D is the spatial dimension. Then any moment is invariant under a change of integration variables, $\boldsymbol{v} = \sqrt{\theta}\boldsymbol{c} + \boldsymbol{u}$, where θ and $\boldsymbol{u}$ are arbitrary,

$$M_{\boldsymbol{n}} = \int f(\boldsymbol{v}, \boldsymbol{x}, t)\boldsymbol{v}^{\boldsymbol{n}} d^D \boldsymbol{v} \tag{26}$$

$$= \int f\left(\sqrt{\theta}\boldsymbol{c} + \boldsymbol{u}, \boldsymbol{x}, t\right)(\sqrt{\theta}\boldsymbol{c} + \boldsymbol{u})^{\boldsymbol{n}} \theta^{D/2} d^D \boldsymbol{c}. \tag{27}$$

Thus, if the moments are evaluated with a quadrature with Q abscissas, it follows

$$M_{\boldsymbol{n}} = \sum_{i=1}^{Q} f_i^\lambda(\boldsymbol{x}, t)(\sqrt{\theta}\boldsymbol{c}_i + \boldsymbol{u})^{\boldsymbol{n}}, \tag{28}$$

with $\boldsymbol{n}$ in a certain range. In LBM, Gauss-Hermite quadrature would be a popular choice, where the Gaussian weight parametrically depends on the gauge $\lambda = \{\boldsymbol{u}, T\}$. Gauge-invariance of all the available moments in Eq. (3) of the main text thus postulates the same independence on the change of integration variables. While this is a triviality in the continuous-velocity case, it becomes a well-defined condition in the discrete-velocity setting.

TWO-DIMENSIONAL DECAYING TURBULENCE

We report the simulation of decaying two-dimensional turbulence. A grid resolution of $N = 1024$ grid points per dimension and a Reynolds number $Re = N\sqrt{2E_0}/\nu = 1.3134 \cdot 10^4$ are chosen to ensure that the standard LBGK is reasonably resolved (see [3] for the description of the setup). The mean initial kinetic energy and enstrophy are denoted by E_0 and Z_0, respectively and the eddy turnover time is defined as $t_e = Z_0^{-1/2}$. Snapshots of the vorticity field and of energy spectra at various times are compared with the standard LBGK in Fig. 2 and Fig. 3, respectively. While the snapshots of vorticity agree well, even though are not identical as in any turbulent flow simulation with different methods, energy spectra are in excellent agreement.

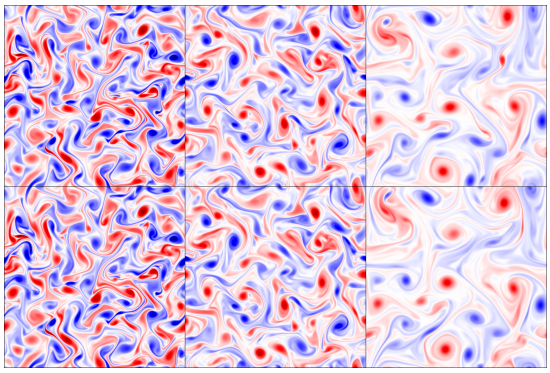

FIG. 2. Simulation of decaying two-dimensional turbulence. Snapshots of vorticity field for three time instances. Top row: D2Q9 standard LGBK; Bottom row: D2Q9 present method; Left: $t = 10t_e$; Center: $t = 20t_e$; Right: $t = 50t_e$.

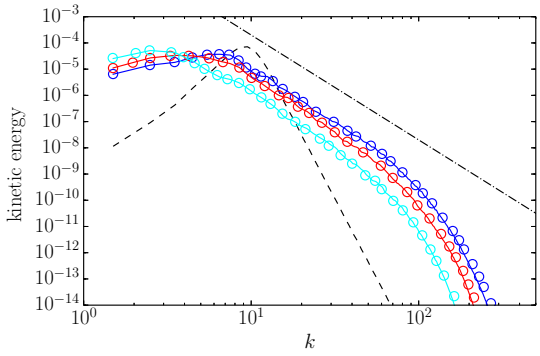

FIG. 3. Energy spectrum of decaying homogeneous two-dimensional turbulence. Circles: LBGK; Line: present method. Blue: $t = 10t_e$; Red: $t = 20\ t_e$; Light blue: $t = 50t_e$. Dashed line: Initial energy spectrum. Dot-dashed line: k^{-3} power law.

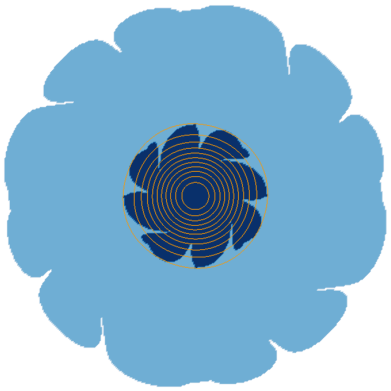

FIG. 4. Instantaneous recording of a standing vortex with rotation Mach number $\mathrm{Ma}_v = 0.8$. Colors indicate number of iterations required for convergence of predictor-corrector scheme (white: 1, light blue: 2, dark blue: 3). Lines: density contours.

PREDICTOR-CORRECTOR SCHEME

The number of predictor-corrector iterations depends on the flow and initial seed gauges, however, unique solution is found independent of the initial guess values. On average three iterations lead to convergence, which is defined for iteration $n + 1$ of field ϕ by

$$|\phi_{n+1} - \phi_n| < \epsilon_{\mathrm{abs}} + \epsilon_{\mathrm{rel}}\phi_{n+1}, \tag{29}$$

where absolute tolerance $\epsilon_{\mathrm{abs}} = 10^{-12}$ and relative tolerance $\epsilon_{\mathrm{rel}} = 10^{-10}$ are used in the simulations. Convergence criterion (29) must be separately fulfilled for $\phi = \{u_x, u_y.\sqrt{\theta}\}$. Fig. 4 shows the number of iterations at a particular instant in time for the standing vortex with vortex Mach number $\mathrm{Ma}_v = 0.8$ (see main text for definition of the flow). Superimposed density contours indicate the center of the vortex. It is apparent that generally more iterations are needed in regions where the flow changes rapidly, and thus, initial seed values based on the previous time step (Eqs. (7) and (8) in the main text) are farther from the converged result. A maximum number of 5 iterations was recorded for high advection Mach numbers $\mathrm{Ma}_a \approx 100$.

CONVERGENCE ORDER

Convergence with respect to grid resolution of the present method was tested using the Green-Taylor vortex flow. Analytical solution of the flow field is given by

$$u_x(\boldsymbol{x}, t) = -(u_0/\sqrt{2})\cos(kx)\sin(ky)\exp(-2\nu k^2 t), \tag{30}$$
$$u_y(\boldsymbol{x}, t) = (u_0/\sqrt{2})\sin(kx)\cos(ky)\exp(-2\nu k^2 t), \tag{31}$$

with wave number $k = 2\pi/L$ and domain size L. In order to maintain incompressibility, a small character-

istic Mach number $\mathrm{Ma} = u_0/\sqrt{T} = 0.001$ was chosen and the simulation was run at isothermal conditions $T = 3T_L = 1$. Thus, the speed of sound is $\sqrt{3}$ times larger than in a standard LBM simulation with the same lattice. Initial density was set to unity, $\rho_0 = 1$, and simulated flow field is compared to with respect to theoretical prediction. Fig. 5 shows the rate of convergence of the relative error averaged over a time period $[0.9t_h, 1.1t_h]$, where t_h is the half-decay time. The present scheme recovers second order of accuracy, which coincides with standard LBM and its semi-Lagrangian variant.

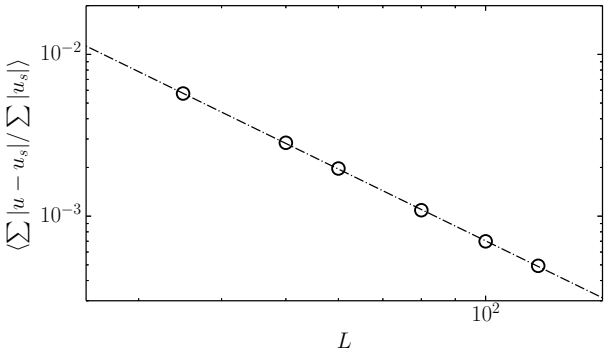

FIG. 5. Convergence rate of Green-Taylor vortex flow for grid resolutions $L \in [35, 120]$ and Reynolds number $\mathrm{Re} = u_0 L/\nu = 50$. Symbols: relative error with respect to solution $\boldsymbol{u}_s$; Line: second order convergence.

the sound precursor (upper sound pressure peak) and the second sound propagate radially from the vortex center with time. Moreover, the peak sound corresponding to the maximum pressure decays with time, for both the precursor and the second sound. Note that the nonlinear acoustics is typically a small (about 1%) perturbation on top of the main hydrodynamic pressure. Excellent comparison is evident between the DNS [4], the ELBM in the co-moving reference frame with $D2Q49$ speeds [5] and the present method with $D2Q25$ speeds.

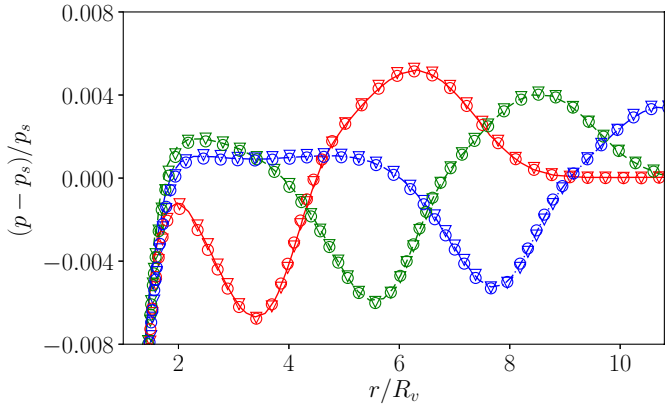

FIG. 6. Radial sound pressure measured at an angle $\theta = -45^\circ$ with respect to x-axis for times $t = 6$ (red), $t = 8$ (green), $t = 10$ (blue). Line: DNS [4]. Triangle: ELBM [5]. Circle: present.

SOUND PRESSURE IN VORTEX-SHOCK INTERACTION

A two-dimensional vortex characterized by the Mach number $\mathrm{Ma_v} = 0.25$ is advected at the inflow Mach number $\mathrm{Ma_a} = 1.2$ and subsequently interacts with a stationary planar shock. Details on the numerical setup can be found in [4]. In Fig. 6 we compare the sound pressure $\Delta p = (p - p_\mathrm{s})/p_\mathrm{s}$, where p_s is the pressure behind the shock wave. The sound pressure distribution in Fig. 6 was measured in the radial direction with the origin at the vortex center, at the angle $\theta = -45^\circ$ with respect to the x-axis and at different non-dimensional times $t = 6, 8, 10$. From the plot one can notice how both

* Present address: California Institute of Technology, Pasadena, CA 91125, USA
† Corresponding author; karlin@lav.mavt.ethz.ch

[1] N. Prasianakis, S. Chikatamarla, I. Karlin, S. Ansumali, and K. Boulouchos, Mathematics and Computers in Simulation **72**, 179 (2006).
[2] X. B. Nie, X. W. Shan, and H. D. Chen, Europhys. Lett. **81**, 34005 (2008).
[3] F. Bösch, S. S. Chikatamarla, and I. Karlin, ESAIM: Proceedings and Surveys **52**, 1 (2015).
[4] O. Inoue and Y. Hattori, J. Fluid Mech. **380**, 81 (1999).
[5] N. Frapolli, S. S. Chikatamarla, and I. V. Karlin, Phys. Rev. Lett. **117**, 010604 (2016).